Supporting Information

for

Abnormal in-plane stretchability of two-dimensional metal-organic framework

Dong Fan,[a,*] Aydin Ozcan,[b] Pengbo Lyu,[c] Guillaume Maurin[a,*]

[a] *ICGM, Univ. Montpellier, CNRS, ENSCM, Montpellier, 34095, France*

[b] *TUBİTAK Marmara Research Center, Materials Technologies, Gebze, Kocaeli, 41470, Turkey*

[c] *Hunan Provincial Key Laboratory of Thin Film Materials and Devices, School of Material Sciences and Engineering, Xiangtan University, Xiangtan, 411105, People's Republic of China*

*Email: dong.fan@cnrs.fr (D.F); guillaume.maurin1@umontpellier.fr (G.M)

Index **Page**

Supporting Tables

Table S1 | Lattice parameters and corresponding atomic bond lengths of the DFT-optimized $NiF_2(pyz)_2$ models using different functionals.

Functional	a [Å]	b [Å]	α (β) [°]	d_{Ni-N} [Å]	d_{Ni-F} [Å]	d_{C-C} [Å]	d_{C-N} [Å]	d_{C-H} [Å]
PBE[1]	6.964	6.964	90	2.092	2.006	1.393	1.346	1.093
PBE+*U*[1–3]	7.061	7.061	90	2.143	1.959	1.395	1.344	1.093
PBE+*U*+D3[1–4]	7.018	7.018	90	2.124	1.966	1.394	1.343	1.093
PBEsol[5]	6.840	6.840	90	2.039	1.991	1.390	1.342	1.098
revPBE[6]	7.075	7.075	90	2.139	2.012	1.398	1.350	1.092

Table S2 | Data preparation for the MLP training of the 2D $NiF_2(pyz)_2$ MOF framework.

Types	Supercell	Number of snapshots
Pristine (structural optimization and AIMD runs at 100 K-300K)	1 × 1 / 3 × 3	16866
1% isotropic compression (100 K-300K)	3 × 3	3000
1% isotropic stretch (100 K-300K)	3 × 3	3000
Tensile strain ((100 K-300K, including two different directions)	3 × 3	14929
Total		37795

Supporting Figures

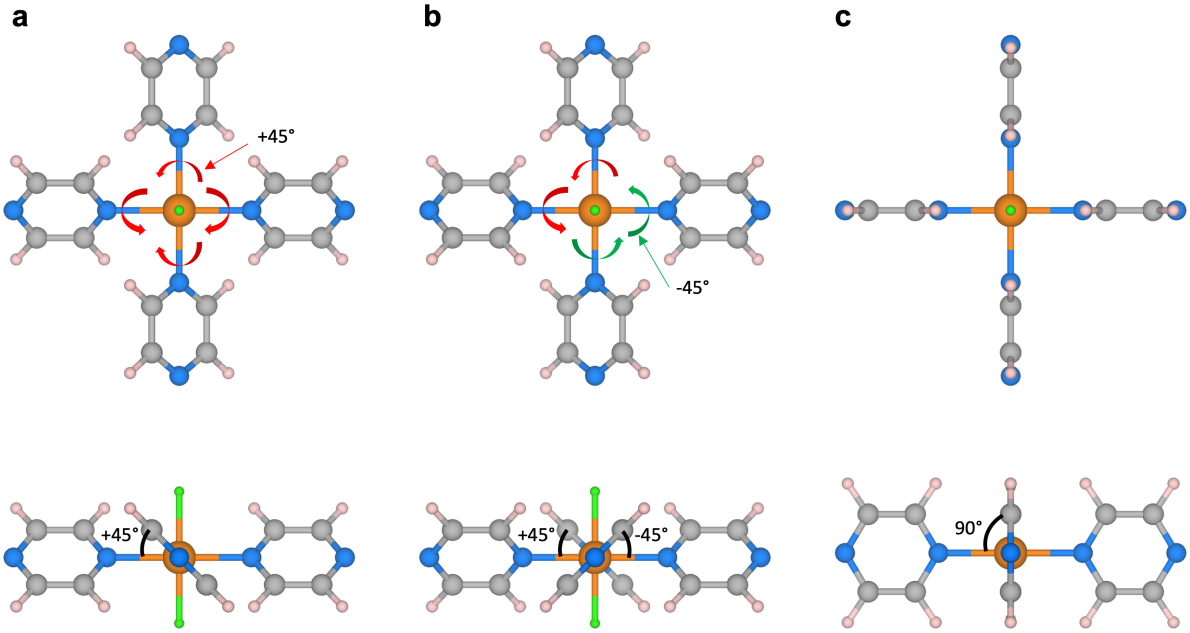

Fig. S1 | Three possible initial configurations of the 2D periodic $NiF_2(pyz)_2$, (**a**) C_2h, (**b**) D_4h, and (**c**) *P4/mmm* symmetry, respectively. Ni is shown in orange, N in blue, F in green, H in light pink, and C in dark-gray. The cell lattice is not shown in the illustration.

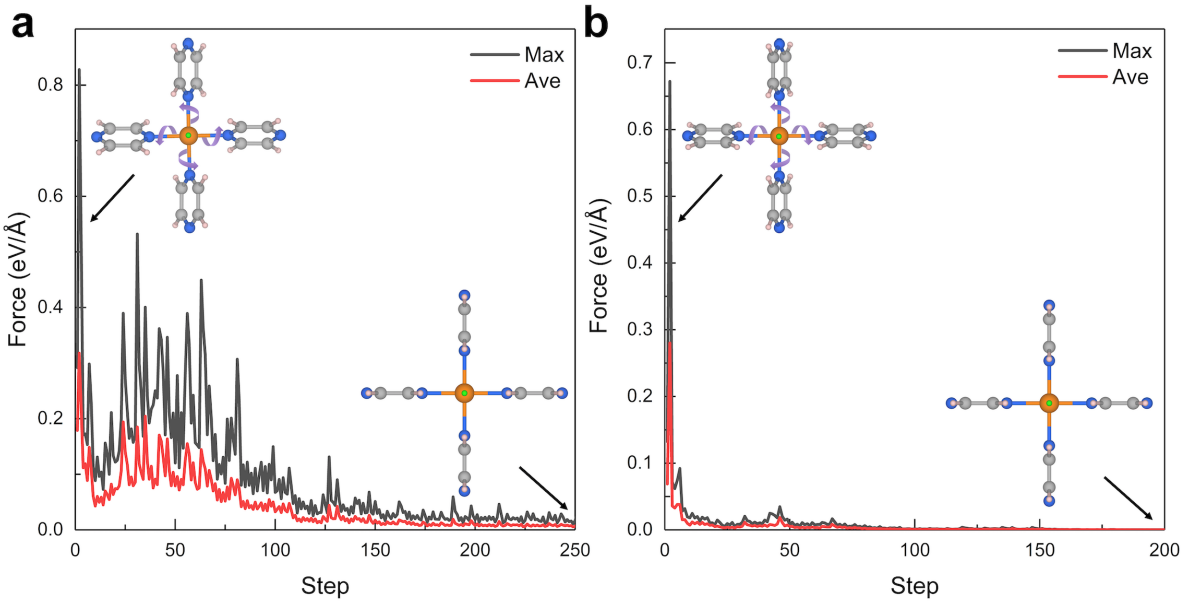

Fig. S2 | Profiles of force changes during the DFT-geometry optimization for two symmetrical configurations, (**a**) C_2h and (**b**) D_4h symmetry, respectively. The insets represent the configurations before and after DFT-geometry optimization. Ni is shown in orange, N in blue, F in green, H in light pink, and C in dark-gray. The cell lattice is not shown in the illustration.

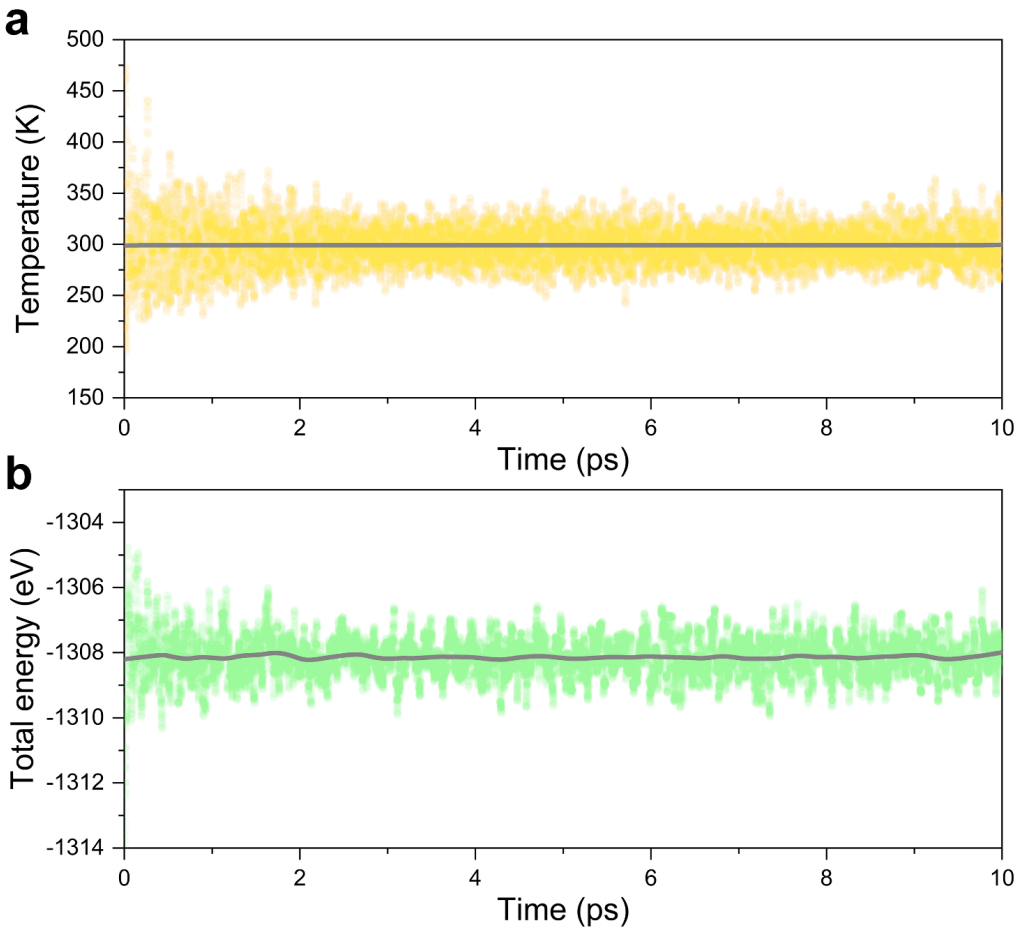

Fig. S3 | Evolution of (a) temperature and (b) total energy obtained by *ab initio* molecular dynamics (AIMD) simulations for $NiF_2(pyz)_2$ (3 × 3 supercell). AIMD simulations for 10 ps in the NVT ensemble (T=300 K) and a timestep of 0.5 fs.

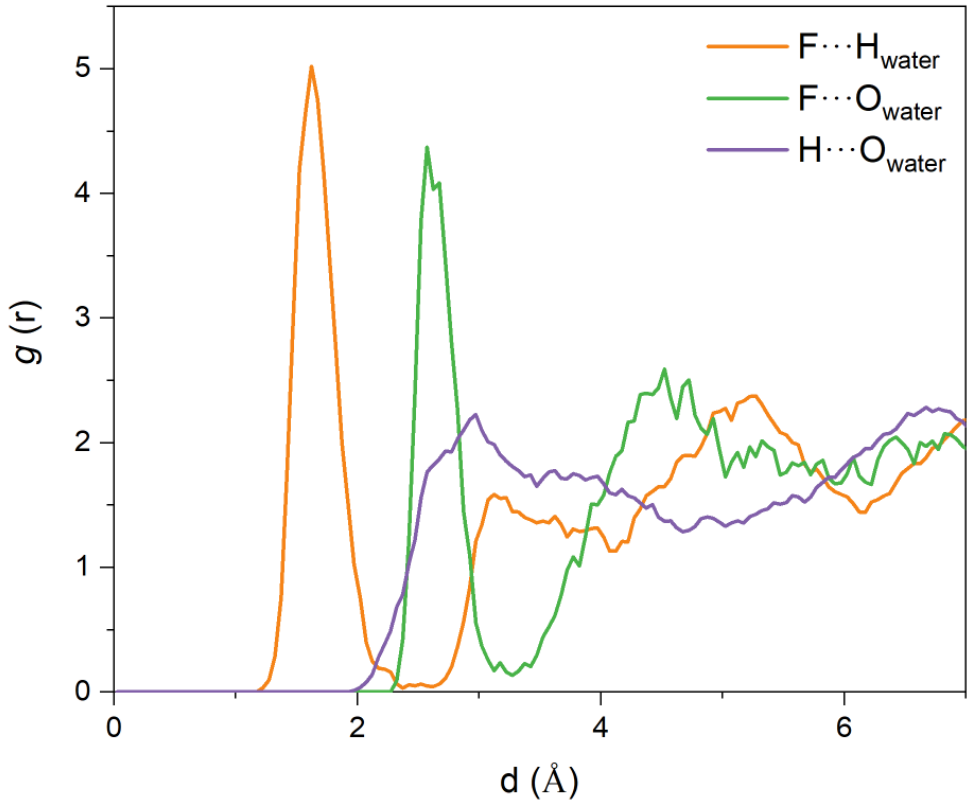

Fig. S4 | Radial distribution functions (RDFs) calculated from AIMD simulations at 300 K between diverse atoms of 2D $NiF_2(pyz)_2$ and water atoms.

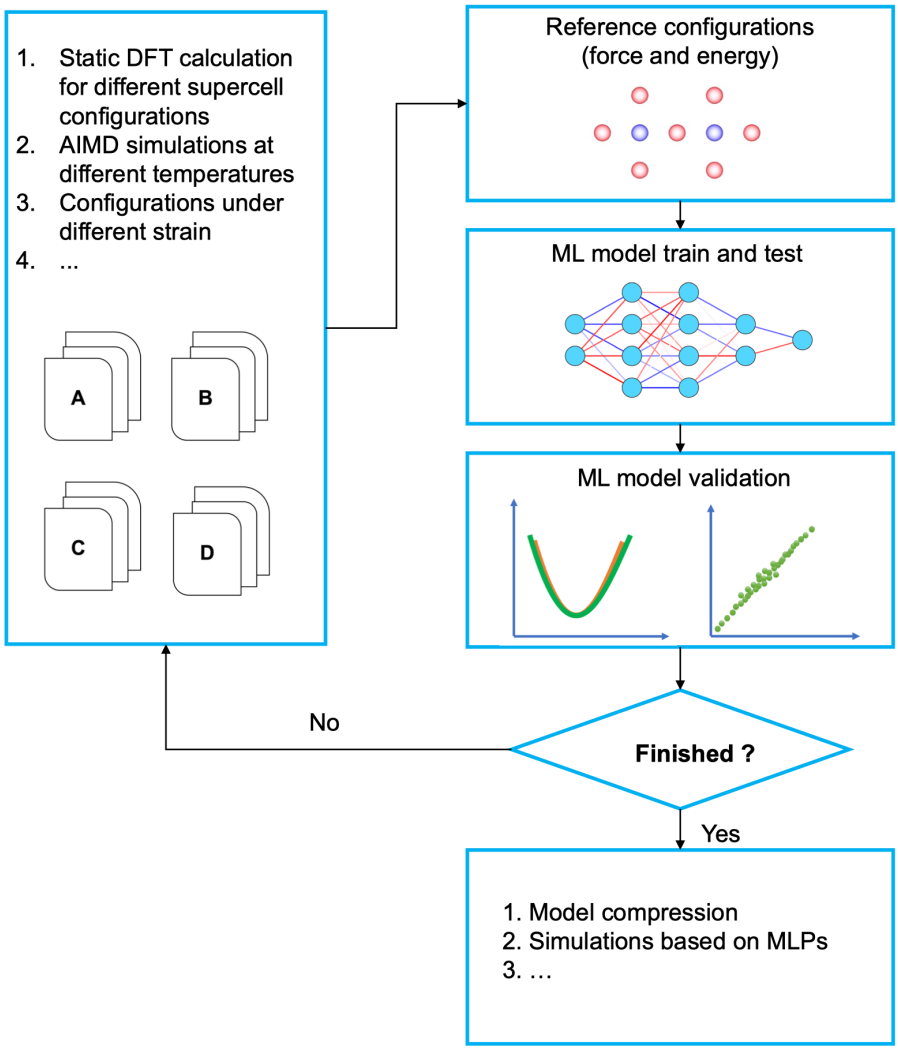

Fig. S5 | Overview of the methodology to derive the MLP for the 2D MOF.

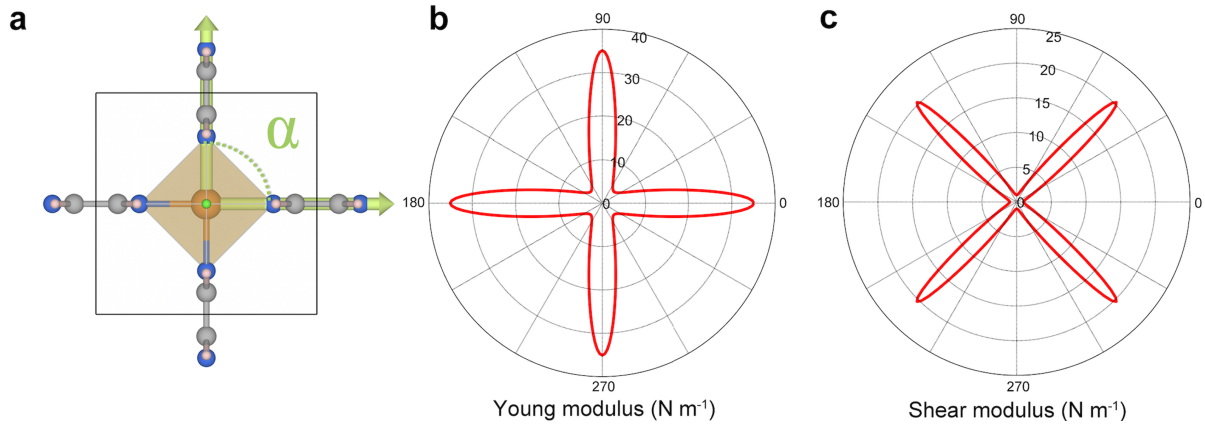

Fig. S6 | (**a**) Crystal structure of the DFT-optimized $NiF_2(pyz)_2$ from top view. ***α*** represents the angle of N–Ni–N in the framework. Polar diagrams for the (**b**) Young's modulus and (**c**) shear modulus of the 2D $NiF_2(pyz)_2$, respectively. Ni is shown in orange, N in blue, F in green, H in light pink, and C in dark-gray. The black line represents unit cell.

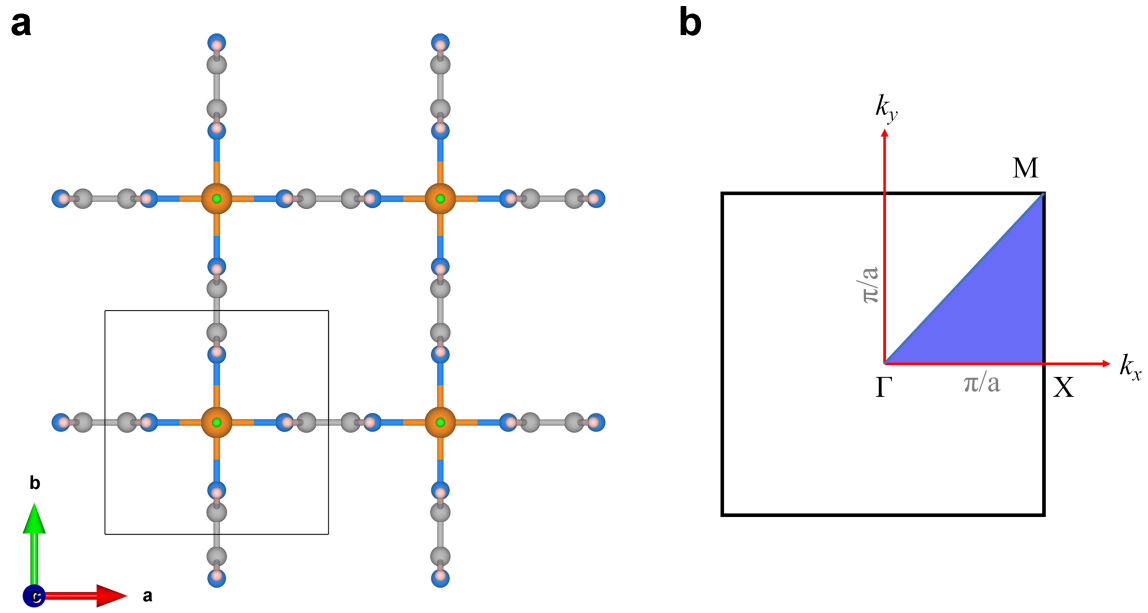

Fig. S7 | (**a**) Top view of the DFT-optimized 2D $NiF_2(pyz)_2$ and corresponding (**b**) two-dimensional Brillouin zone with the symmetry points Γ (0.0, 0.0, 0.0), X (0.5, 0.0, 0.0) and M (0.5, 0.5, 0.0), respectively. The highlighted triangle is known as the reduced Brillouin zone.

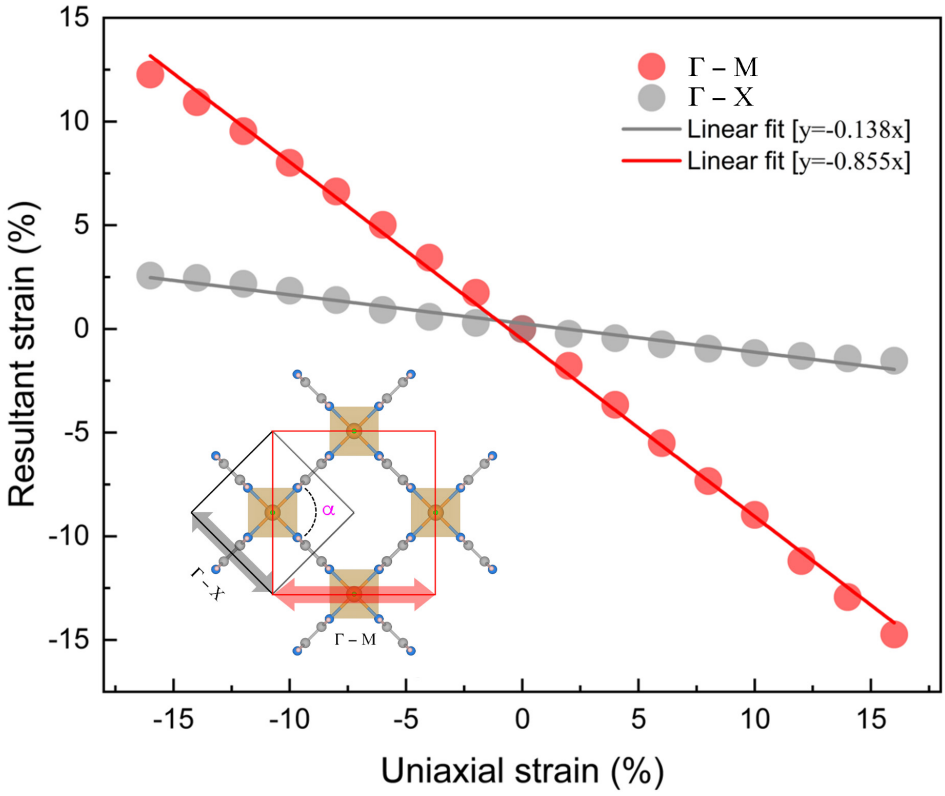

Fig. S8 | Resultant strain induced by the uniaxial strain (including stretch and compression deformations) along Γ-X and Γ-M directions. Ni is shown in orange, N in blue, F in green, H in light pink, and C in dark-gray. The red and black lines represent the unit cell. The values are based on DFT calculations, where the uniaxial tensile strain is obtained by fixing the value in strain direction and fully relaxed in the opposite direction during the structural optimisation process to reach the valid lattice parameters. The approach is implemented by recompiling the VASP package.

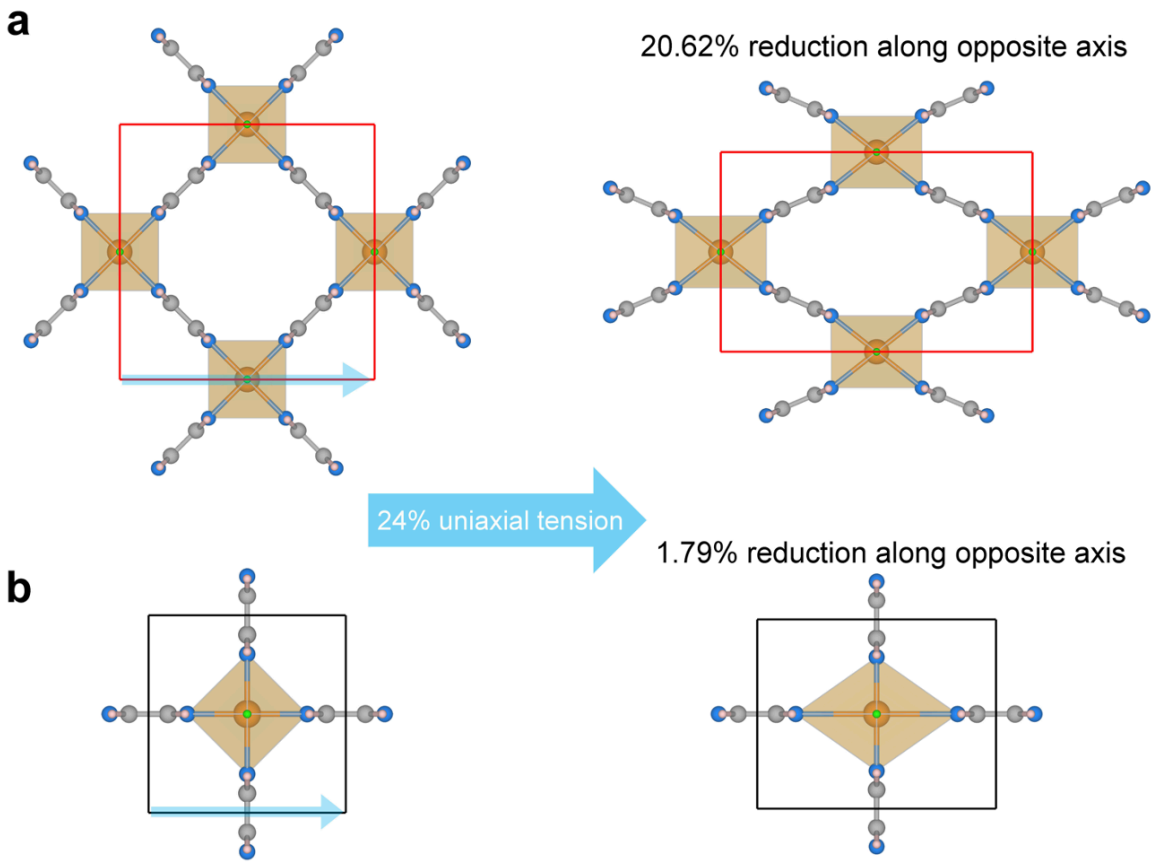

Fig. S9 | Schematic diagram of 24% tensile strain applied along (**a**) Γ-M and (**b**) Γ-X axis directions for 2D $NiF_2(pyz)_2$, respectively. Ni is shown in orange, N in blue, F in green, H in light pink, and C in dark-gray. The red and black lines represent the unit cell. The values are based on DFT calculations, where the uniaxial tensile strain is obtained by fixing the value in strain direction (blue arrow) and fully relaxed in the opposite direction during the structural optimisation process to reach the valid lattice parameters.

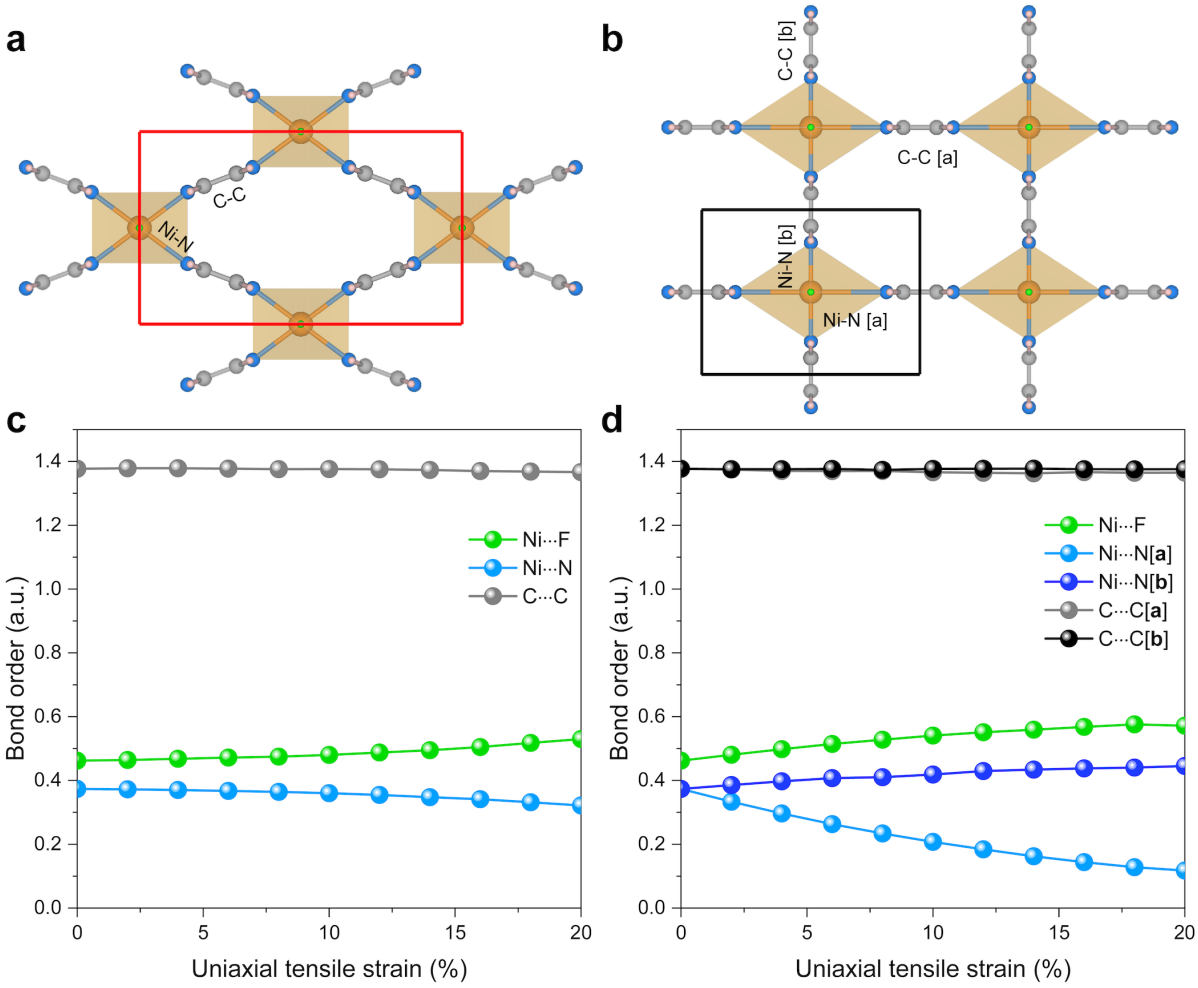

Fig. S10 | Schematic diagram of uniaxial tensile strain applied along the (**a**) Γ-M and (**b**) Γ-X directions, respectively, and the corresponding (**c**, **d**) bond order changes. Ni is shown in orange, N in blue, F in green, H in light pink, and C in dark-gray. The red and black lines represent the unit cell. The strained structures are derived from DFT calculations where the uniaxial tensile strain was determined by fixed value in the strain direction and completely relaxed in the opposing direction during the structural optimization. The resulting fully optimised configurations are used to conduct bond order analyses. The bond order between atoms was computed by using CHARGEMOL program.[7]

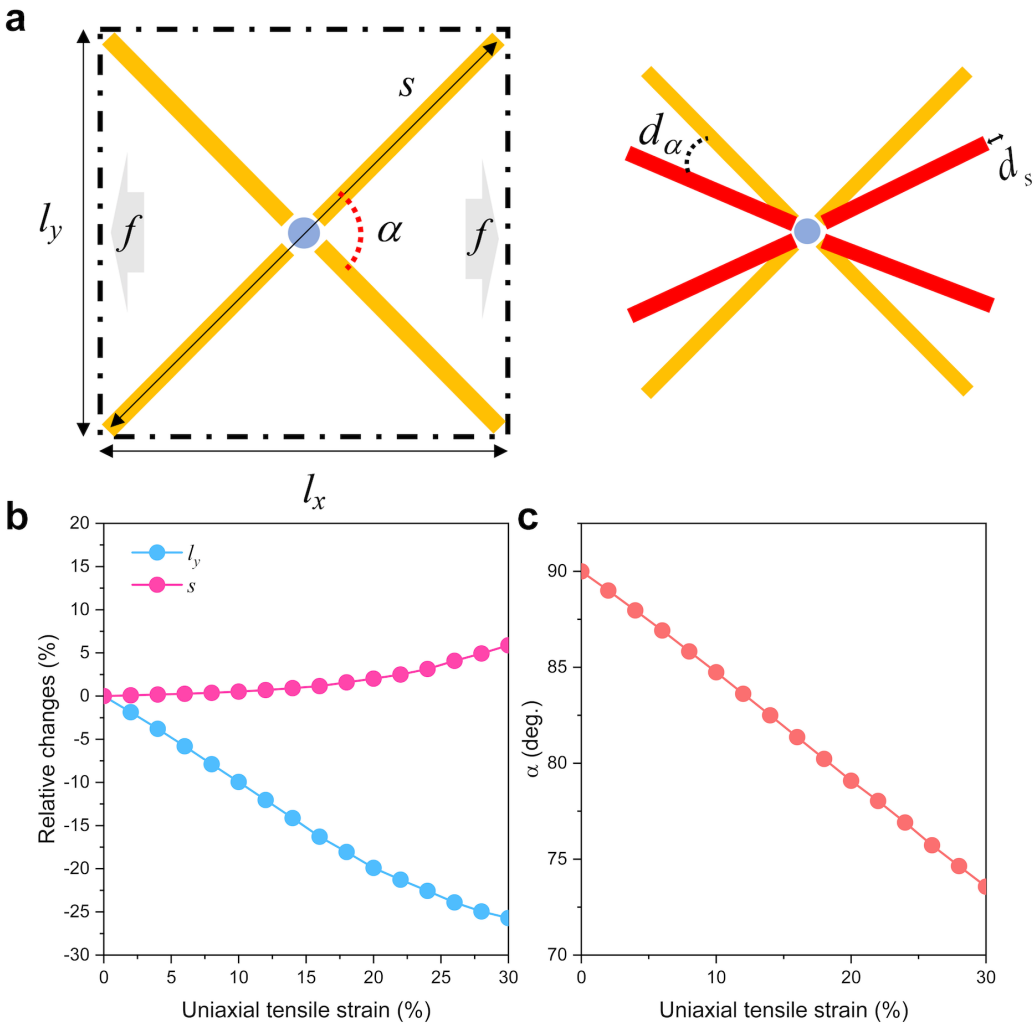

Fig. S11 | (**a**) Simplified deformation mechanism of $NiF_2(pyz)_2$ under tensile strain along the Γ-M direction. The tensile strain arises from two distinct deformation modes: rotation and elongation. Here, f denotes the applied force on the lattice, S represents the length of the rods along the diagonal direction, and α signifies the in-plane angle between two diagonal rods. d_α and d_s denote the change of α and S, respectively; l_x and l_y represent the lattice length in the horizontal and vertical directions, respectively. (**b**, **c**) The variation of l_y, S, and α of the $NiF_2(pyz)_2$ with respect to the uniaxial tensile strain. The data are based on DFT calculations, where the uniaxial tensile strain is obtained by fixing the value in strain direction and fully relaxed in the opposite direction during the structural optimisation process to reach the valid lattice parameters.

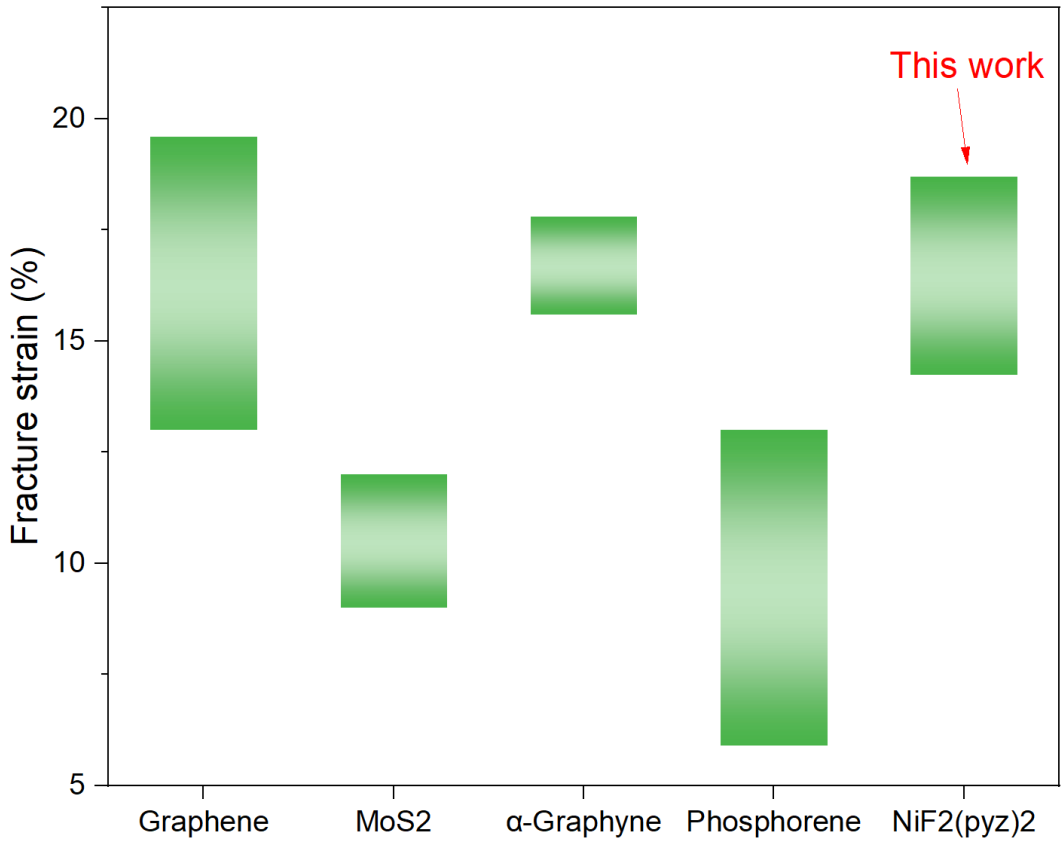

Fig. S12 | Fracture strain of the 2D $NiF_2(pyz)_2$ and some of other 2D materials (Collected from Refs. [8–11]) at room temperature (300 K). For fracture strain of the 2D $NiF_2(pyz)_2$, the values are extracted from the result of MLP-MD simulations at 300 K, as shown in Figure 3 in the main text.

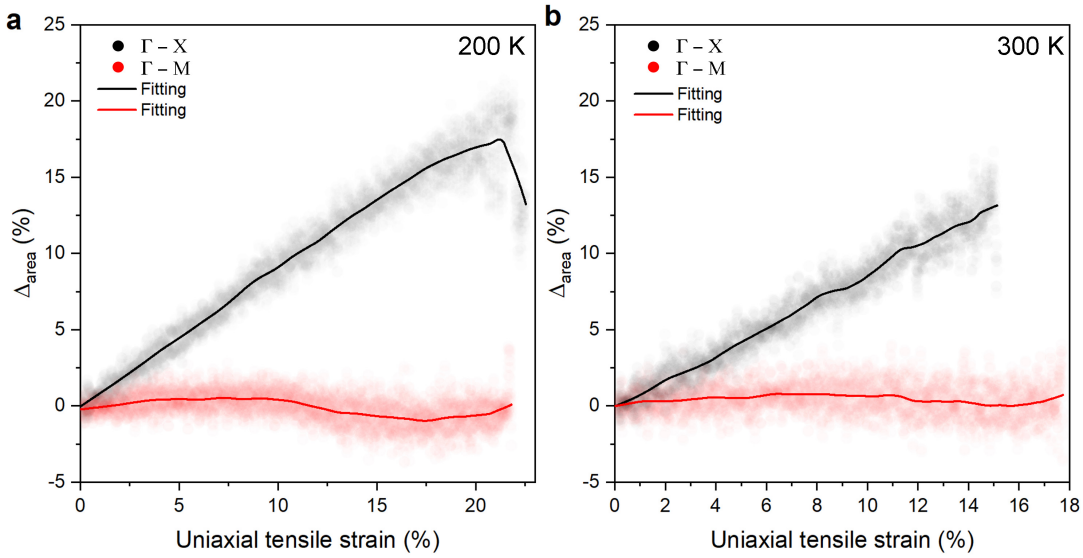

Fig. S13 | The Δ_{area} under a strain deformation along the two different directions at (**a**) 200 and (**b**) 300 K using MLP-MD simulations. The coloured dots represent the MLP-MD simulation data points, and the solid lines represent the corresponding fitted data.

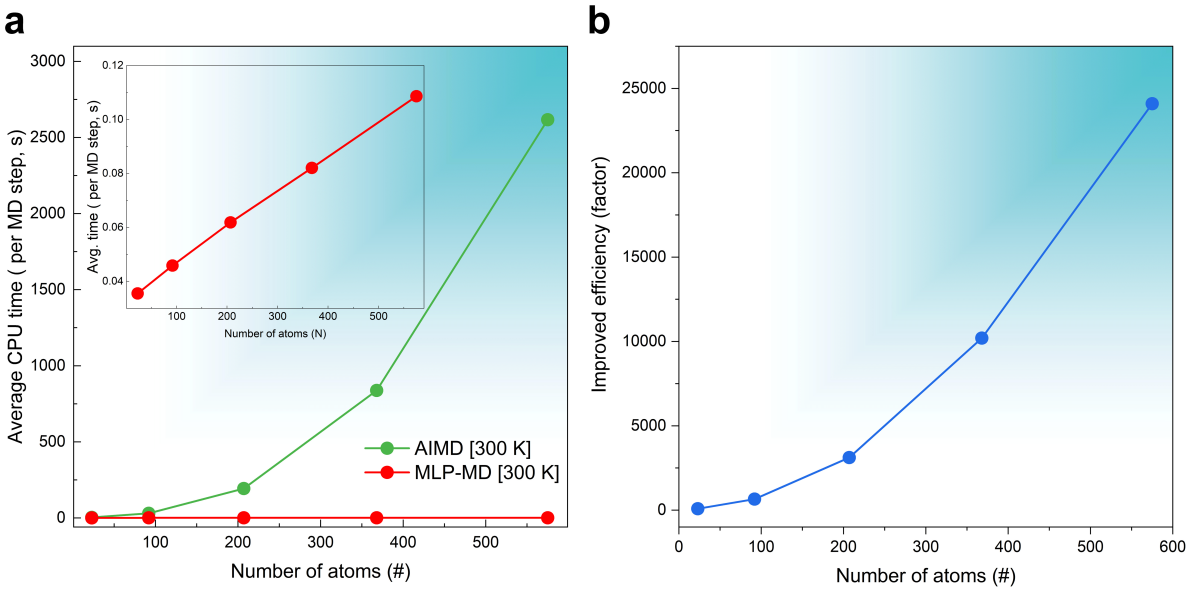

Fig. S14 | (**a**) Computing CPU time comparison between DFT and MLP MD calculations. For each system (the simulation cell from 23 to 575 atoms), the same CPU (64-cores) was used to compute the average time per MD time step in seconds. When compared to AIMD, (**b**) illustrates the efficiency boost through the MLP-MD method.

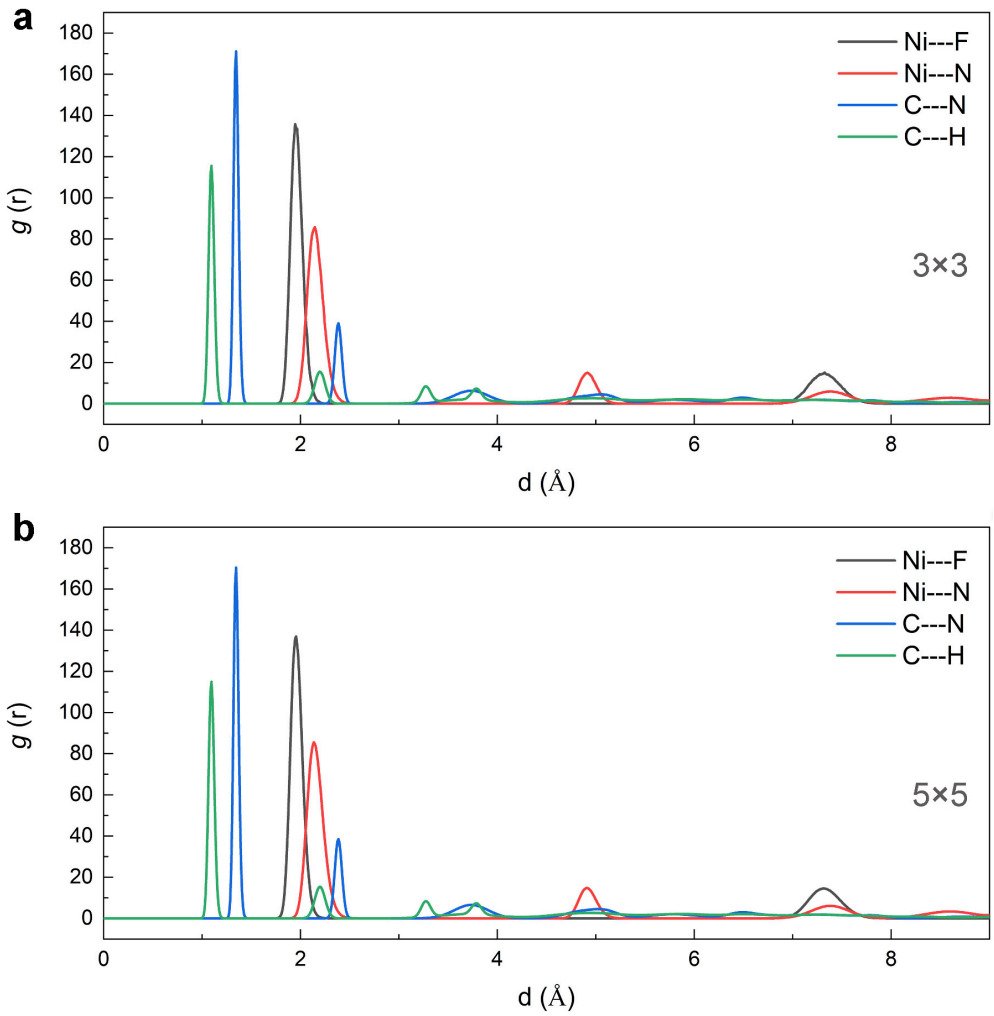

Fig. S15 | Comparison of the RDFs calculated for different atom pairs of the 2D $NiF_2(pyz)_2$ with different supercells: (a) 3 × 3 and (a) 5 × 5 supercells using MLP- MD simulations at 300 K.

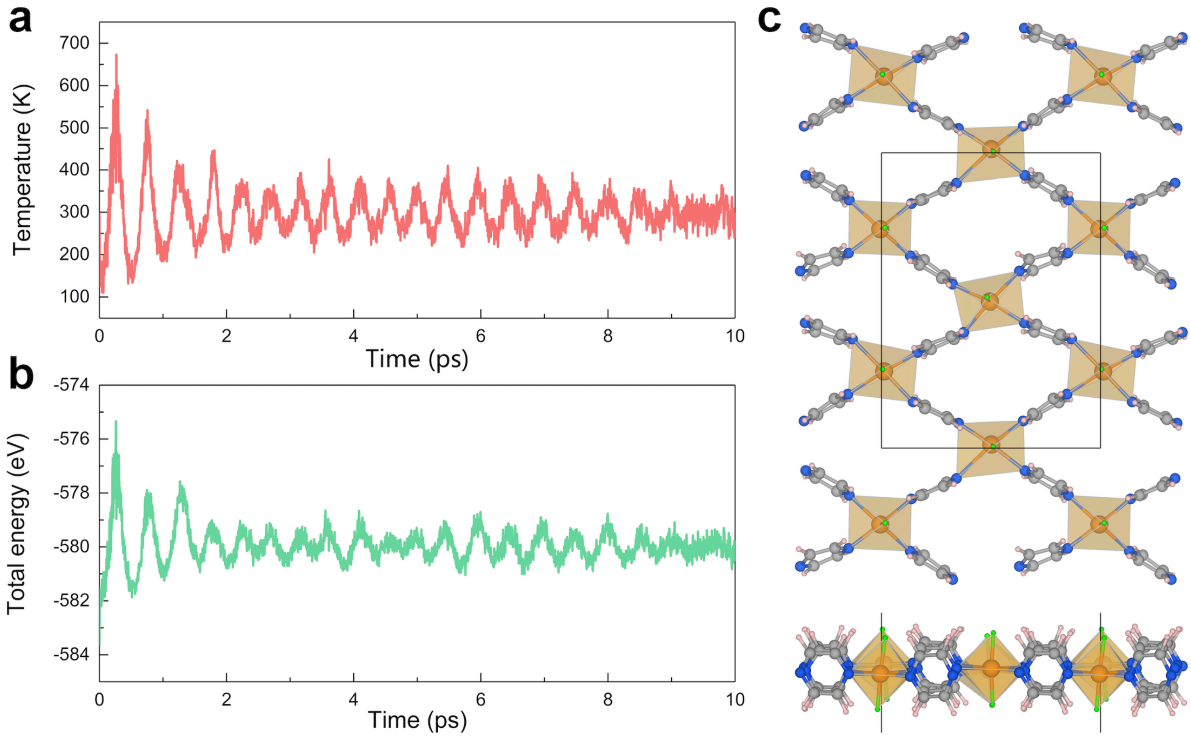

Fig. S16 | Evolution of (**a**) Temperature and (**b**) total energy of the 2D $NiF_2(pyz)_2$ under 22% tensile strain along Γ-M direction over time during the AIMD simulations at 300 K. (**c**) Snapshot of the corresponding structure (top and side views) after 10 ps simulation. Ni is shown in orange, N in blue, F in green, H in light pink, and C in dark-gray. The black line represents unit cell.

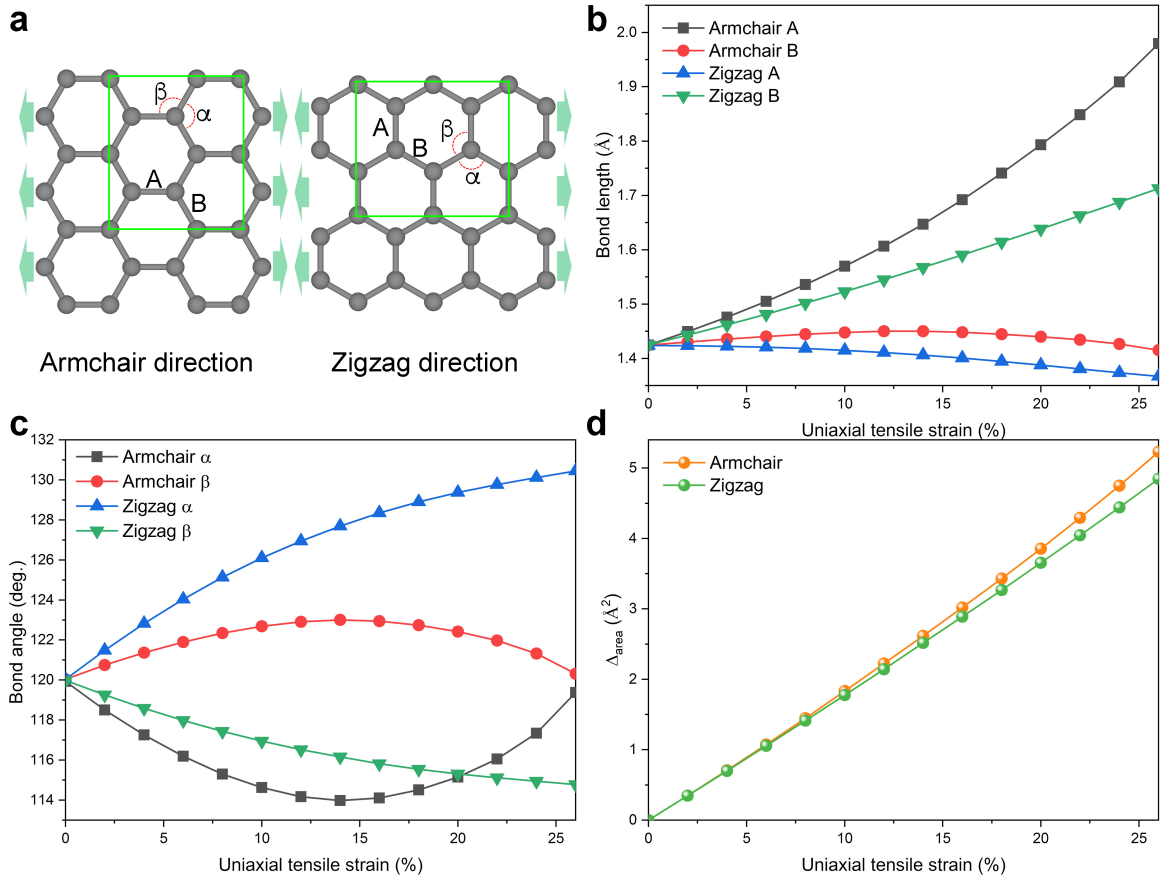

Fig. S17 | (a) A graphene model under uniaxial tensile test in the armchair and zigzag direction, respectively. Variation of (**b**) bond length and (**c**) bond angle as a function of uniaxial strain when a tension is applied on along zigzag and armchair directions. The bond lengths of A and B were referred to as Zigzag A and Zigzag B, respectively, when tension was applied along the zigzag direction; Similarly, the bond lengths of A and B were referred to as Armchair A and Armchair B, respectively, when tension was applied along the armchair direction; the bond angles of α and β were referred to as Zigzag α and Zigzag β, respectively, when tension was applied along the zigzag direction. Armchair α and Armchair β were used to refer to the bond angle of α and β when tension was applied along the armchair direction. (**d**) The relative in-plane area changes under a strain deformation along armchair and zigzag directions, respectively.

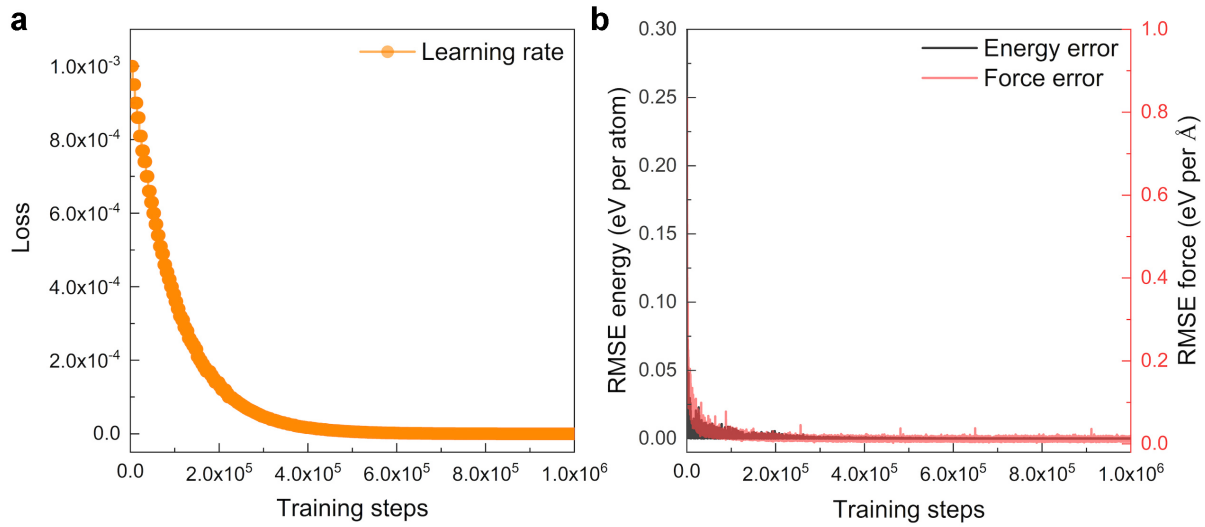

Fig. S18 | (**a**) Training loss with the steps. (**b**) Variation of RMSE of force and energy with training steps.

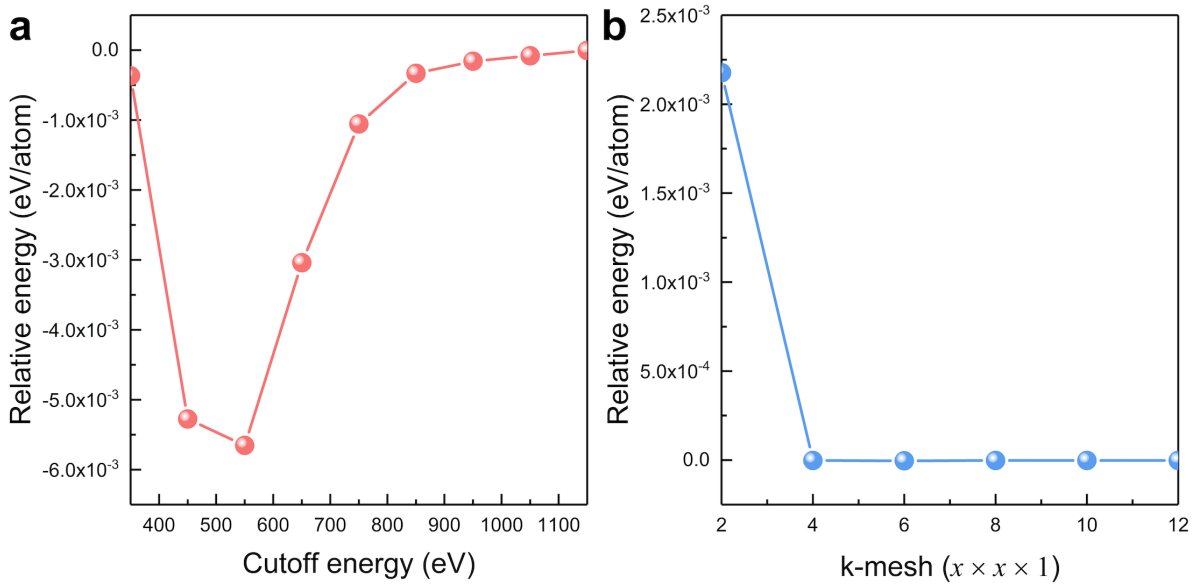

Fig. S19 | Convergence test of the DFT calculation, including the (**a**) cut-off energy and (**b**) *k*-point test. The final choice of cut-off energy and *k*-points are 900 eV and 6 × 6 × 1, respectively. An optimised unit cell structure of 2D $NiF_2(pyz)_2$ based on DFT+U approach is adopted.

Supporting Notes

Structural stability of $NiF_2(pyz)_2$ in aqueous solution

A key characteristic of MOF structures that allows for industrial applications is its stability in aqueous conditions, as many industrial processes, such as gas separation, gas storage, desalination *etc*., involve MOFs being stable in water environment.[12] Unfortunately, most MOFs (*e.g.* MOF-5[13]) are unstable in water vapor, which makes future commercialization endeavours more challenging.[14,15] We therefore used *ab-initio* molecular dynamics (AIMD) simulations to investigate the stability of $NiF_2(pyz)_2$ in aqueous solution. The DFT-D3 method of the Grimme van der Waals correction[4] was also used to account for the long-range interactions in the simulations. The total length of the simulation was set to 5 ps, the time step was set to 0.5 ps with a NVT ensemble at 300 K. The final energy fluctuation with simulation time is shown in Figure 1e of the main text. It can be seen that no significant abrupt change in total energy is observed throughout the AIMD simulations, while the structure remains unchanged after 5 ps, as shown in Figure 1f, evidencing the excellent thermodynamic stability of our proposed configuration even in aqueous solution. The calculated RDFs between water atoms and framework atoms are very close to that of the aqueous solution with the fluoride ions,[16] as shown in Fig. S4, demonstrating that our AIMD process describes the interaction between the $NiF_2(pyz)_2$ and the aqueous solution accurately. Therefore, the high hydrolytic stability of $NiF_2(pyz)_2$ provides the possibility to subsequently explore applications based on this material in others fields.

Mechanical properties of $NiF_2(pyz)_2$ and comparison with other materials

We performed DFT calculations to determine the elastic constants first, which were found to be $C_{11} = C_{22} = 39.92$ N m^{-1}, $C_{12} = C_{21} = 5.44$ N m^{-1}, and $C_{66} = 0.99$ N m^{-1}. Therefore, the mechanical stability of the $NiF_2(pyz)_2$ can be evaluated based on the Born criteria[17] for 2D tetragonal materials, which state that the standard mechanical stability is achieved when $C_{11}C_{22} - C_{12}^2 > 0$ and $C_{66} > 0$. Based on these criteria, we can conclude that the $NiF_2(pyz)_2$ is indeed mechanically stable. Based on elastic constants, Young's modulus (Y_α) and Poisson's ratio (ν_α) of $NiF_2(pyz)_2$ along in-plane α can be obtained by the following expression:

$$Y_\alpha = \frac{C_{11}C_{22} - C_{12}^2}{C_{11}\sin\alpha^4 + A\sin\alpha^2\cos\alpha^2 + C_{22}\cos\alpha^4}$$

$$\nu_\alpha = \frac{C_{12}\sin\alpha^4 + B\sin\alpha^2\cos\alpha^2 + C_{12}\cos\alpha^4}{C_{11}\sin\alpha^4 + A\sin\alpha^2\cos\alpha^2 + C_{22}\cos\alpha^4}$$

Where $A = {(C_{11}C_{22} - C_{12}^2)}/{C_{66}} - 2C_{12}$ and $B = C_{11}+C_{22} - (C_{11}C_{22} - C_{12}^2)/C_{66}$. The calculated angular-dependence results are presented in Fig. S6. Additionally, fundamental mechanical property of ν_α, which is characterized by the negative ratio of transverse strain to axial strain during loading, the ν_α values obtained using the linear fitting method are in excellent agreement with those calculated using the elastic constants, as shown in Fig. S8. The small Poisson's ratio found in the *a*-plane direction (α=0°, as shown in Figure 3d of the main text) of the structure suggests its length in the opposite direction can remain a very small change as compared to α=45° (corresponds to the tensile deformation along the Γ-M direction, as discussed in the main text).

Origin of the in-plane anisotropy of the 2D $NiF_2(pyz)_2$

To investigate the origin of this in-plane anisotropy more deeply, we computed the typical bond order between atoms in the 2D $NiF_2(pyz)_2$ structure, which mainly involves the bonding strength between the metal node and the ligand (Ni–N), and between the ligand itself (C–C). Bond order is a useful tool for predicting the stability and properties of molecules/solids, such as their strength and reactivity. As shown in Fig. S10, the C–C bond order remains nearly unchanged (~1.37 Å) during the process of the applied tension strain, whether the strain is applied along the Γ-M or Γ-X direction, indicating that the structural deformation upon the application of a strain has negligible effect on the ligand (pyrazine) moiety. It is also interesting to mention that, the bond strength between the metal node and the ligand (Ni–N) changes equally and smoothly along the Γ-M deformation (*cf.* Fig. S10c). It is observed that during the strain along the Γ-X direction, the Ni-N bond decreases more drastically along the tension direction, while it increases slowly perpendicular to the tensile direction (*cf.* Fig. S10d). However, for the deformation along the Γ-M direction, the Ni-N bond order only decreases by 13% even at 20% strain (69% reduced along Γ-X direction). This suggests that the drastic change in topology during the tension strain applied in the Γ-M direction compared to that in the Γ-X direction leads to a slowly decreasing metal-ligand bond strength, which eventually leads to very different in-plane mechanical responses in the two different directions when the uniaxial tensile strain is applied.

In-plane deformation mechanism of 2D $NiF_2(pyz)_2$ along Γ-M direction using mechanical modelling

In this section we investigate only the in-plane deformation mechanism of 2D $NiF_2(pyz)_2$ under tension along Γ-M direction by using mechanical modelling. Considering its structural characteristics, we can approximate the pyrazine ligands as the connecting rods, and the metal nodes as the intersection position of the connecting rods. (Refer to Figure 3 of the main text) To illustrate this concept, Fig. S11 demonstrates the simplified geometric model, where the pyrazine ligands are simplified as straight rods, and the metal nodes as a hinge that connects two cross rods.

Within this simplified model, the overall deformation of the 2D $NiF_2(pyz)_2$ under tension strain can be attributed to two mechanisms: stretching and/or rotation of the rods.[18] Nevertheless, as shown in the Fig. S11b, our calculations show that the length of the connecting rod changes very little during the entire uniaxial strain loading processes, we can approximate that the structural changes during the uniaxial strain loading come mainly from the change of the pinch angle of the rods (α). We also observe here that the variation of the α angle is consecutive, as shown in Fig. S11c, which means that the structural changes during the tensile process are completely mechanical torsion, without any structural phase transition. Therefore, a wide range of applications are expected in areas such as ultra-thin mechanical sensors and flexible wearable devices *etc*.[19–22]

Dataset collection for machine learning potential (MLP) construction of the 2D MOF

For the dataset that was not under any strain we mainly trained by collected structural information from AIMD simulations. The total number of collected structural databases was 14,788 of which 13,788 databases were used for training, and 1,000 for validation (temperatures ranging from 100-300K). To train the machine learning potential (MLP) for the uniaxial tensile process of the 2D $NiF_2(pyz)_2$ at a finite temperature, the corresponding structural information is required to be presented during the training process. We then collected a total of 37,795 structural information, which contains 22,866 pristine 2D $NiF_2(pyz)_2$ configurations as well as 5,435 configurations at 10% strain (Γ-X direction) and 9,494 configurations in the Γ-M direction (temperatures ranging from 100-300K). Relevant details are summarised in Table S2.

Performance and transferability of the MLP at different sizes

We have demonstrated that the MLP developed in this work predicts the properties of 2D $NiF_2(pyz)_2$ with near DFT accuracy, even for the different temperatures and system sizes. We also examined the computational efficiency of the MLP by using a 64-core AMD Rome CPU (2.6 GHz) fixed computational resources. We tested the scale-up of MLP by comparing the CPU time required for 1000 MD time steps for the $NiF_2(pyz)_2$ system from 23 to 575 atoms. The results are shown in Fig. S14a, where an almost linear scaling is observed. It can be observed that for DFT calculations, the time for molecular dynamics simulations increases significantly with the number of atoms in the simulated system, while for MLP, the computations are extremely accelerated, as shown in Fig. S13b. This is why MLP-based molecular dynamics simulation can manage tens of thousands of atoms as well as nanosecond-level simulations. The rough testing-calculation shows that even for the complex chemical systems [five different elements for 2D $NiF_2(pyz)_2$], MLP is able to maintain computational accuracy at the DFT scale while still being computationally efficient.

The transferability of the machine learning force field at different sizes was also examined. Fig. S15 shows the RDFs based on NVT simulations at 300 K for two different sizes. It can be clearly seen that the RDF locations and the shape of the peaks are almost the same for the two different systems, demonstrating the excellent transferability of the trained MLP and the high agreement between the simulated results and the DFT results (*cf.* Figure 2g in the main text).

Stability of 2D $NiF_2(pyz)_2$ under uniaxial tension

The stability of the structure after tensile deformation was also investigated, as shown in Fig. S16, by conducting a long-time AIMD simulation at room temperature for 10 ps with the same parameter settings as before. It can be seen that the energy fluctuations are stable during the simulation, demonstrating that the proposed configuration is still stable even under tensile deformation of up to 22%.

Mechanical response of graphene under uniaxial tension

It is well known that when a uniaxial tensile strain is applied to a two-dimensional material, the surface area of the material increases as the tensile strain increases below the fracture strain. Here, as a benchmark for the calculation methodology, we explored the structural response to tensile strain using first principles calculations for the example of graphene. As shown in Fig. S17, we investigated the evolution of representative bond lengths (*tpye*-A and *type*-B) and bond

angles (α and β) in the graphene under uniaxial tensile strain. Not surprisingly, we find that under the tensile strain loading, the lattice parameter in the other axial direction decreases, and therefore the corresponding bond lengths become shorter. It is also worth to note that our results are highly consistent with previous findings in the literature,[23] except for the bond length of *type*-A (cf. Fig. S17) along the Γ-M direction. The main reason for this discrepancy maybe due to the fact that the previous work with the empirical approach (AIREBO potential)[24] which may fails to reasonably describe the structural changes during deformation. Overall, our results show good consistency with the work based empirical force field method. Additionally, we calculate the change in surface area (Δ_{area}) during tensile strain, and we find that the Δ_{area} increases linearly with increasing applied strain, for both Γ-X and Γ-M directions. The benchmark calculations for graphene system show that the calculation method used in this study is able to correctly describe the structural changes during the deformation, demonstrating the applicability of the calculation method used in this work.

Training process of the machine learning potential (MLP)

Throughout the MLP training process, the exponential reduction of the root mean squared error (RMSE) value was quantified. Fig. S18 displays the loss function and RMSE values during the training process. Given the nature of DFT data and other factors that influence network operation, the RMSE for force and energy may approach a value close to zero, but it is unlikely to reach an ideal value of zero. We also found that the trained RMSE results can achieve the accuracy of the DFT scale.

Convergence test of the DFT calculations

Convergence testing is extremely important in first-principles calculations, as such calculations usually involve complex numerical calculations that require control over both numerical error and convergence.[25] If the numerical error is too large or the convergence is poor, the results of the calculation will become unreliable. As shown in Fig. S19, we tested the convergence of the cut-off energy and *k*-points for the unit cell of 2D $NiF_2(pyz)_2$. It can be seen that the system is less sensitive to the variation of the k-point, however for the cut-off energy, the conventional 520 eV[26,27] is not sufficient, therefore we finally used 900 eV in all the DFT calculations presented in this paper.

Supporting Reference

1. Perdew, J. P., Burke, K. & Ernzerhof, M. Generalized Gradient Approximation Made Simple. *Phys. Rev. Lett.* **77**, 3865–3868 (1996).
2. Ylvisaker, E. R., Pickett, W. E. & Koepernik, K. Anisotropy and magnetism in the LSDA + U method. *Phys. Rev. B* **79**, 035103 (2009).
3. Emery, A. A. & Wolverton, C. High-throughput DFT calculations of formation energy, stability and oxygen vacancy formation energy of ABO3 perovskites. *Sci Data* **4**, 170153 (2017).
4. Grimme, S. Semiempirical GGA-type density functional constructed with a long-range dispersion correction. *J. Comput. Chem.* **27**, 1787–1799 (2006).
5. Perdew, J. P. *et al.* Restoring the Density-Gradient Expansion for Exchange in Solids and Surfaces. *Phys. Rev. Lett.* **100**, 136406 (2008).
6. Zhang, Y. & Yang, W. Comment on "Generalized Gradient Approximation Made Simple". *Phys. Rev. Lett.* **80**, 890–890 (1998).
7. Manz, T. A. & Limas, N. G. Introducing DDEC6 atomic population analysis: part 1. Charge partitioning theory and methodology. *RSC Adv.* **6**, 47771–47801 (2016).
8. Sha, Z.-D., Pei, Q.-X., Ding, Z., Jiang, J.-W. & Zhang, Y.-W. Mechanical properties and fracture behavior of single-layer phosphorene at finite temperatures. *J. Phys. D: Appl. Phys.* **48**, 395303 (2015).
9. Zhang, Y. Y., Pei, Q. X. & Wang, C. M. Mechanical properties of graphynes under tension: A molecular dynamics study. *Appl. Phys. Lett.* **101**, 081909 (2012).
10. Jiang, J.-W. Parametrization of Stillinger–Weber potential based on valence force field model: application to single-layer MoS_2 and black phosphorus. *Nanotechnology* **26**, 315706 (2015).

11. Zhang, Z. *et al.* Accelerated discoveries of mechanical properties of graphene using machine learning and high-throughput computation. *Carbon* **148**, 115–123 (2019).
12. Wang, C., Liu, X., Keser Demir, N., Chen, J. P. & Li, K. Applications of water stable metal–organic frameworks. *Chem. Soc. Rev.* **45**, 5107–5134 (2016).
13. Kaye, S. S., Dailly, A., Yaghi, O. M. & Long, J. R. Impact of Preparation and Handling on the Hydrogen Storage Properties of Zn_4O(1,4-benzenedicarboxylate)$_3$ (MOF-5). *J. Am. Chem. Soc.* **129**, 14176–14177 (2007).
14. Liu, B., Vikrant, K., Kim, K.-H., Kumar, V. & Kailasa, S. K. Critical role of water stability in metal–organic frameworks and advanced modification strategies for the extension of their applicability. *Environ. Sci.: Nano* **7**, 1319–1347 (2020).
15. Batra, R., Chen, C., Evans, T. G., Walton, K. S. & Ramprasad, R. Prediction of water stability of metal–organic frameworks using machine learning. *Nat Mach Intell* **2**, 704–710 (2020).
16. Schran, C. *et al.* Machine learning potentials for complex aqueous systems made simple. *Proc. Natl. Acad. Sci. U.S.A.* **118**, e2110077118 (2021).
17. Born, M., Huang, K. & Lax, M. Dynamical Theory of Crystal Lattices. *American Journal of Physics* **23**, 474–474 (1955).
18. Ying, P. *et al.* Tension-induced phase transformation and anomalous Poisson effect in violet phosphorene. *Materials Today Physics* **27**, 100755 (2022).
19. Akinwande, D., Petrone, N. & Hone, J. Two-dimensional flexible nanoelectronics. *Nat Commun* **5**, 5678 (2014).
20. Wang, Y. *et al.* Giant Poisson's Effect for Wrinkle-Free Stretchable Transparent Electrodes. *Adv. Mater.* **31**, 1902955 (2019).
21. Iqbal, S. M. A., Mahgoub, I., Du, E., Leavitt, M. A. & Asghar, W. Advances in healthcare wearable devices. *npj Flex Electron* **5**, 9 (2021).

22. Lin, Z., Huang, Y. & Duan, X. Van der Waals thin-film electronics. *Nat Electron* **2**, 378–388 (2019).

23. Zhao, H., Min, K. & Aluru, N. R. Size and Chirality Dependent Elastic Properties of Graphene Nanoribbons under Uniaxial Tension. *Nano Lett.* **9**, 3012–3015 (2009).

24. Stuart, S. J., Tutein, A. B. & Harrison, J. A. A reactive potential for hydrocarbons with intermolecular interactions. *The Journal of Chemical Physics* **112**, 6472–6486 (2000).

25. Lejaeghere, K. *et al.* Reproducibility in density functional theory calculations of solids. *Science* **351**, aad3000 (2016).

26. Jain, A. *et al.* Commentary: The Materials Project: A materials genome approach to accelerating materials innovation. *APL Materials* **1**, 011002 (2013).

27. Singh, A. K., Montoya, J. H., Gregoire, J. M. & Persson, K. A. Robust and synthesizable photocatalysts for CO2 reduction: a data-driven materials discovery. *Nat Commun* **10**, 443 (2019).

Supporting Movies

Movie S1. [http://www.fandong.org/2d_mof_S1.html]

Raman_vibration_mode_595.mov

Calculated Raman-active mode of the $NiF_2(pyz)_2$ at 595 cm^{-1}

Movie S2. [http://www.fandong.org/2d_mof_S2.html]

Raman_vibration_mode_1039.mov

Calculated Raman-active mode of the $NiF_2(pyz)_2$ at 1039 cm^{-1}

Movie S3. [http://www.fandong.org/2d_mof_S3.html]

Raman_vibration_mode_3119.mov

Calculated Raman-active mode of the $NiF_2(pyz)_2$ at 3119 cm^{-1}

Movie S4. [http://www.fandong.org/2d_mof_S4.html]

Movie_S4_AIMD_water.mov

Structural oscillation of the $NiF_2(pyz)_2$ supercell with water during the AIMD simulation at 300 K

Movie S5. [http://www.fandong.org/2d_mof_S5.html]

Movie_S5_100K_G-M.mov

Structural evolution with uniaxial strain applied along the Γ-M direction using MLP-based MD simulation at 100 K

Movie S6. [http://www.fandong.org/2d_mof_S6.html]

Movie_S6_100K_G-X.mov

Structural evolution with uniaxial strain applied along the Γ-X direction using MLP-based MD simulation at 100 K

Movie S7. [http://www.fandong.org/2d_mof_S7.html]

Movie_S7_300K_NVT_11132_atoms.mov

Structural oscillation of the $NiF_2(pyz)_2$ supercell (11132 atoms) during the MLP-based MD simulation at 300 K